The International Journal of Advanced Manufacturing Technology (2019) 101:2259–2273
https://doi.org/10.1007/s00170-018-3117-0

ORIGINAL ARTICLE

Grindability of powder metallurgy nickel-base superalloy FGH96 and sensibility analysis of machined surface roughness

Benkai Li[1] · Wenfeng Ding[1] · Changyong Yang[1] · Changhe Li[2]

Received: 21 August 2018 / Accepted: 20 November 2018 / Published online: 29 November 2018

Abstract
The grindability and sensibility analysis of surface roughness of powder metallurgy nickel-base superalloy FGH96 were studied in comparison to the wrought nickel-base superalloy GH4169. The effects of grinding parameters (such as workpiece infeed speed, depth of cut, and abrasive wheel speed) on grinding force, grinding temperature, specific grinding energy, abrasive wheel wear, and surface roughness were analyzed. The results show that the grinding force, grinding temperature, and specific grinding energy of GH4169 are usually higher than those of FGH96 under the given experimental conditions. However, the wear behavior of the brown corundum abrasive wheels when grinding these two kinds of nickel-base superalloy material is generally identical. The sensitivity of GH4169 workpiece surface roughness to depth of cut and workpiece infeed speed is higher than that of FGH96, but the sensitivity of GH4169 to abrasive wheel speed is less than that of FGH96. Finally, it is inferred that the grinding performance of FGH96 is slightly better than that of GH4169.

Keywords Grindability · Nickel-base superalloy · Grinding force, grinding temperature, specific grinding energy, surface roughness · Sensibility analysis

1 Introduction

Nickel-base superalloys, at present, are widely used in aero-engine components owing to their good strength, thermal stability, thermal ductility, fatigue resistance, and corrosion resistance [1–3]. For example, the wrought nickel-base superalloy GH4169 has become the most widely used material. Grinding is usually worked as the last machining procedure of nickel-base superalloy, which has an important effect on the machining accuracy and quality of parts [4]. Based on this point, it is necessary to study the grinding performance of nickel-base superalloy material in order to provide a technical support for grinding of aero-engine turbine disk. On the other hand, the nickel-base superalloys are the typical difficult-to-cut material. During the grinding process, nickel-base superalloys have the characteristics of large grinding force and high grinding temperature, serious abrasive wheel wear, high energy consumption, and poor surface integrity of workpiece [5–7]. In addition, the hardening layer, residual stress, white layer, and grain deformation are also easily produced on the surface of nickel-base superalloy materials [8]. Therefore, it is full of great significance to deeply study the grindability of nickel-base superalloy materials.

In the recent years, a series of research work has been carried out to detect the machinability of the different nickel-base superalloy. Du et al. [9–11] conducted milling and cutting experiments of FGH95 superalloy materials. It was found that the cutting speed would affect the surface integrity of the workpiece seriously, and the white layer thickness and microhardness of the machined surface increase with the increasing of cutting speed. Meanwhile, the thickness of plastic deformation layer decreases with the increasing of cutting speeds. The orthogonal grinding experiment of GH4169 superalloy materials was carried out by Huddedar et al. with different abrasive wheels under varied feed speed and depth of cut [12], in which the effect of depth of cut and abrasive grain size on ground surface roughness was rather significant. Furthermore, Qian et al. [13] carried out the comparative grinding experiments of K4125 and Inconel 718 superalloy materials. Under the given experimental conditions, the grinding force and temperature

✉ Wenfeng Ding
dingwf2000@vip.163.com

[1] College of Mechanical and Electrical Engineering, Nanjing University of Aeronautics and Astronautics, Nanjing 210016, China

[2] School of Mechanical Engineering, Qingdao University of Technology, Qingdao 266520, China

produced during grinding K4125 were higher than those produced during grinding Inconel 718, and the ground surface roughness of K4125 was also obviously higher than that of Inconel 718. The resultant tool wear behavior in case of grinding K4125 was also more serious than that in case of grinding Inconel 718. At the same time, Xi et al. [14] evaluated the grindability of Ti-6Al-4V titanium alloy, Inconel 718 superalloy, and Ti_2AlNb intermetallics, through which it was found that the grinding power and grinding force during grinding Inconel 718 were the highest. Balan et al. [15] carried out experimental research on grinding Inconel 751 superalloy materials under different cooling conditions, i.e., dry and low-temperature minimum quantity lubrication (called Cryo-MQL). The results showed that the Cryo-MQL grinding uses 50% to 65% less energy than dry grinding, which can significantly improve the grinding performance. Jia et al. [16] studied the specific energy and surface roughness of minimum quantity lubrication with mixed vegetable oil-based nanofluids by grinding GH4169. It was discovered that the lowest force ratio and specific energy were obtained using the 8% mass fraction of the soybean/castor mixed oil. Guo et al. [17] conducted the grinding experiment of GH4169 with different mixed vegetable oils, in which castor/soybean oil had the best lubricity comparing with the other mixed oils, such as palm/soybean, palm/castor, and so on. Li et al. [18] investigated the chip morphology of GH4169 under ultrasonic vibration grinding conditions. Generally, the ultrasonic vibration has a greater effect on the morphology of grinding chips compared with the effect of grinding parameters.

Ground surface roughness is a critical parameter to reflect the performance of machined materials. Therefore, many research works have focused on surface roughness. Yao et al. [19] studied the surface roughness of grinding Inconel 718 with a resin cubic boron nitride (CBN) wheel and a single alumina (SA) wheel bonded by vitreous. It was reported that the better surface was obtained by using a SA wheel, and the surface roughness was R_a 0.112 μm under the condition of depth of cut of 0.005 mm, workpiece infeed speed of 16 m/min, and abrasive wheel speed of 25 m/s. Hecker and Liang [20] established the predictive model for ground surface roughness. The abrasive wheel microstructure and material properties are considered through the chip thickness model. The predicted results show a nice agreement with the experimental results. At the same time, Ding et al. [21] also built the model for predicting the surface roughness. The modeling results of surface roughness agreed with the experimental result well. In addition, the ground surface roughness would be improved with the abrasive wheel wear, which led to that more grains were participated in grinding from the prediction model.

The powder metallurgy nickel-base superalloy FGH96 is a type of damage-tolerant nickel-base superalloy. It has become the first choice material in aero-engine turbine disk because of the excellent characteristic of homogeneous organization, superfine grain, high yield strength, and high elevated temperature fatigue strength [22, 23]. However, the correlative research on grinding of FGH96 has been seldom reported, although research works on grinding operation of nickel-base superalloys, especially for the wrought nickel-base superalloy GH4169, have been carried out. Therefore, for better understanding the processing characteristics, a comparative study on grinding operation of powder metallurgy nickel-base superalloy FGH96 and wrought nickel-base superalloy GH4169 with brown corundum abrasive wheel is proposed in this work. Accordingly, the grindability of FGH96 would be evaluated by analyzing grinding force, specific grinding energy, grinding temperature, and abrasive wheel wear. Particularly, for better understanding the grindability, the sensibility analysis of machined surface roughness is also investigated.

2 Experimental details and procedure

2.1 Workpiece materials

The ground materials were powder metallurgy nickel-base superalloy FGH96 and wrought nickel-base superalloy GH4169. The material properties are listed in Tables 1 and 2. According to Table 1, the element compositions of FGH96 and GH4169 are similar except for individual elements. For example, the elements Mn and Cu were contained in GH4169 material, while not existed in FGH96 material. But from Table 2, the mechanical properties of FGH96 and GH4169 are quite different. The tensile strength and yield strength of GH4169 are resemblant to that of FGH96 at room temperature. However, the tensile strength and yield strength of FGH96 at 750 °C are higher than that of GH4169 at 650 °C, which indicates that FGH96 has a better thermal strength and stability than GH4169 at high temperature. The workpiece size was 25 mm × 30 mm × 5 mm. The surface grinding experiment was conducted with brown corundum abrasive wheel, which has been widely used to grind nickel-base superalloy. The abrasive grains were in the US mesh size 80# and the actual particle diameter range was 160–200 μm. The diameter of the abrasive wheel d_s was 400 mm, and the width b_s was 20 mm.

2.2 Experimental setup

Figure 1 shows the experimental equipment. The BLOHM PROFIMAT MT-408 high-speed surface grinder, whose output power was 45 kW and the maximum spindle speed was 8000 rpm, was used to conduct the grinding experiments. A single point diamond dresser was used to dress the abrasive wheel after each grinding path. The grinding conditions and dressing parameters are listed in Table 3.

Table 1 Composition of FGH96 and GH4169

Elements	Co	Cr	Mo	W	Al	Ti	Nb	B	Zr	C	Ni	Mn	Cu	Fe
FGH96	13	16	4	4	2.2	3.7	0.8	0.01	0.04	0.04	Bal.	–	–	0.1
GH4169	1.0	19	3.1	–	0.95	0.96	5.25	–	–	0.08	53	0.35	0.3	Bal.

2.3 Measuring method

The grinding force was measured by using the Kistler 9317C type three channel piezoelectric dynamometer. The natural frequencies of three directions of dynamometer, that is X, Y, and Z, were 5 kHz, 5 kHz, and 20 kHz, respectively. The tangential and normal grinding forces were, respectively, measured by the X and Z directions of the dynamometer. Grinding temperature was measured by the semi-natural thermocouple. The semi-natural thermocouple is mainly composited by two workpieces, mica plate and constantan wire, shown in Fig. 2. The constantan wire with the diameter 0.02 mm as the positive electrode, while the workpiece as the negative electrode. It should noted that the mica plate plays the most important role that make the workpiece be not in contact with constantan wire, which is the key to the semi-natural thermocouple. In addition, the semi-natural thermocouple was calibrated by E type standard thermocouple. The calibration calculated modes of FGH96 and GH4169 materials were shown in eq. (1) and (2). The grinding force and temperature measuring diagrammatic sketch are shown in Fig. 3. The MAHR M1 surface roughness tester was used to measure the ground surface roughness. The setting parameter of MAHR M1 surface roughness tester: diameter of the tip was 0.2 μm, the filtering was Gaussian filter, and the cut of setting was 0.8 mm. Sensofar S Neox 3D confocal microscopy was used to measuring the ground surface, and the abrasive wheel surface was characterized by using Leica DMC 4500 optical microscope, shown in Fig. 4.

$$\text{For GH4169}: \quad T_{\text{GH4169}} = -0.0482u^2 + 22.434u + 18.985 \tag{1}$$

$$\text{For FGH96}: \quad T_{\text{FGH96}} = -0.0367v^2 + 12.395v + 25.968 \tag{2}$$

where T_{FGH96} and T_{GH4169} were the grinding temperature of FGH96 and GH4169 workpiece materials. The u and v were the measured thermal electromotive force during grinding process.

3 Experimental results and discussion

3.1 Analysis of grinding force

Grinding force is one of the significant parameters to evaluate the grinding characteristic of materials, which has an important influence on the ground surface roughness and abrasive wheel wear. The typical curve of grinding force signal and the influence of depth of cut, workpiece infeed speed, and abrasive wheel speed on the grinding force of FGH96 and GH4169 superalloys materials are shown in Fig. 5. Figure 5a shows the process of grinding workpiece which divides into three regions: cutting in region, stable cutting region, and cutting out region. It is also found from Fig. 5b that the grinding force per unit width of both the two kinds of superalloy materials increases with the increasing of depth of cut when the workpiece infeed speed and abrasive wheel speed keep constant. The difference of tangential grinding force per unit width $\triangle F_t$ is not significant with the increasing of depth of cut, while normal grinding force per unit width difference $\triangle F_n$ increases gradually. For instance, when the depth of cut $a_p = 0.2$ mm, the tangential grinding force per unit width $F_{\text{t-GH4169}} = 5.5$ N/mm, $F_{\text{t-FGH96}} = 4.2$ N/mm, then $\triangle F_t = 1.3$ N/mm; however, $F_{\text{n-GH4169}} = 15.84$ N/mm, $F_{\text{n-FGH96}} = 12.57$ N/mm, then $\triangle F_n = 3.27$ N/mm; when $a_p = 1.5$ mm, $F_{\text{t-GH4169}} = 15.94$ N/mm, $F_{\text{t-FGH96}} = 13.35$ N/mm, then $\triangle F_t = 2.59$ N/mm, and $F_{\text{n-GH4169}} = 58$ N/mm, $F_{\text{n-FGH96}} = 42.73$ N/mm, then $\triangle F_n = 15.27$ N/mm. According to Fig. 5c, when the abrasive wheel speed and depth of cut are fixed, the tangential and normal grinding forces per unit width of GH4169 and FGH96 superalloy materials show a linear increasing trend with increase of the workpiece infeed speed. When $v_s = 25$ m/s and $a_p = 0.5$ mm, with the increasing of workpiece infeed speed from 80 mm/min to 150 mm/min, the tangential and normal grinding forces per unit width increased from 9.12 N/mm and 21.29 N/mm to 12 N/mm and 39.66 N/mm, respectively, and increased by 31.6% and

Table 2 Mechanical properties of FGH96 and GH4169

Materials	Measuring temperature (°C)	Tensile strength σ_b (MPa)	Yield strength $\sigma_{0.2}$ (MPa)	Density ρ (kg/m^3)	Thermal conductivity k (W/m K)
FGH96	20	1520	1200	8255	9.5
	750	1260	1030	–	–
GH4169	20	1502	1360	8280	13.7
	650	1110	980	–	–

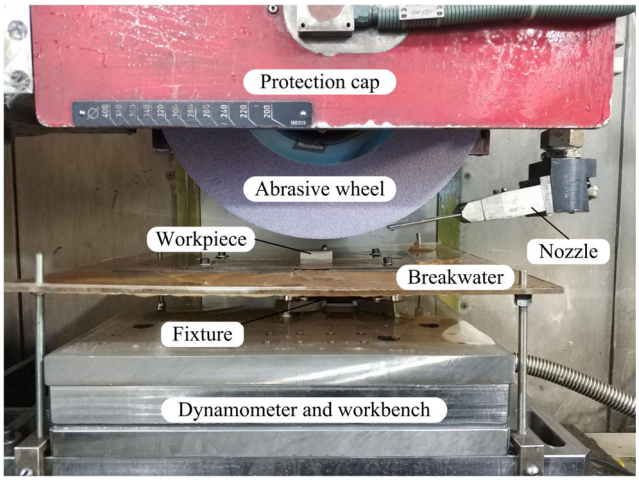

Fig. 1 Experimental equipment

86.3%, respectively. Seen from Fig. 5d, the tangential and normal grinding forces per unit width of GH4169 and FGH96 superalloy materials show a downward trend with the increase of the abrasive wheel speed. When the abrasive wheel speed increases from 20 to 35 m/s, the tangential and normal grinding forces per unit width of GH4169 superalloy material decreased from 10.56 to 7.5 N/mm and from 27.4 to 25.8 N/mm, which decreased by 29% and 6%, respectively. The tangential and normal grinding forces per unit width of FGH96 superalloy material reduced from 8.57 to 5.47 N/mm and from 25.2 and 18.07 N/mm, which decreased by 36.2% and 28.3%, respectively. It finds that the decrease rates of tangential and normal grinding forces per unit width of GH4169 superalloy material (i.e., 29% and 6%, respectively) are generally smaller than that of FGH96 superalloy material (i.e., 36.2% and 28.3%, respectively). From Fig. 5, the normal and tangential grinding force per unit width of GH4169 superalloy are bigger than that of FGH96 superalloy in the case

Table 3 Grinding conditions

Content	Values
Machine tools	Blohm Profimat MT-408 surface grinder
Grinding mode	Surface up-grinding
Abrasive wheel	Brown corundum wheel (80 US Mesh)
Abrasive wheel speed v_s/(m/s)	20, 25, 30, 35
Workpiece infeed speed v_w/(mm/min)	80, 100, 120, 150
Depth of cut a_p/(mm)	1.5, 1.0, 0.5, 0.2
Dressing speed v_d/(m/s)	30
Dressing infeed rate f_d/(mm/min)	200
Dressing depth of cut a_d/(mm)	0.2
Cooling condition	5% emulsified water; 90 L/min, pressure at 1.5 MPa

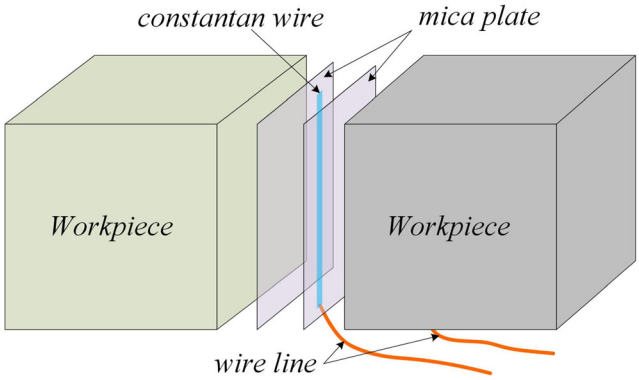

Fig. 2 Semi-natural thermocouple diagrammatic sketch

of the identical grinding parameters. This is because the yield strength of GH4169 superalloy material is higher than that of FGH96 superalloy material, which makes it easier to remove FGH96 superalloy materials during grinding than to remove GH4169 superalloy materials.

During the grinding operation, the variation of grinding force with workpiece infeed speed, abrasive wheel speed, and depth of cut can be qualitatively analyzed based on dynamic active abrasive grain number in the workpiece-wheel contact zone. The average cutting force of a single grain that was assumed during grinding is F_{gt}, so the tangential grinding force was expressed as [24]

$$F_t = F_{gt} \cdot N_d \cdot A \tag{3}$$

$$N_d = k\left(\frac{6V}{\pi d_g^3}\right)^{2/3}\left(\frac{v_w}{v_s}\right)^{1/3}\left(\frac{a_p}{d_s}\right)^{1/6} \tag{4}$$

where A is the area of the grinding arc zone; N_d is the number of dynamic active abrasive grains of abrasive wheel per unit area; k is the constant, $k = 1.2$; V is the volume ratio of the abrasive grains in the abrasive wheel; d_g is the average diameter of the abrasive grain particle, $d_g = 180$ μm; d_s is the abrasive wheel diameter.

According to formula (4), when the abrasive wheel parameters are fixed, the number of dynamic active abrasive grains in the grinding zone increases with the increase of workpiece infeed speed and depth of cut, but decreases with the increasing of abrasive wheel speed. Therefore, according to formula (3), normal and tangential grinding force increases with the increasing of workpiece infeed speed and depth of cut, but decreases with the increasing of abrasive wheel speed.

3.2 Analysis of specific grinding energy

The specific grinding energy represents the energy consumed by grinding per unit volume materials, which is also one of the most important parameters for evaluating the grinding performance of the workpiece material. It has an important influence

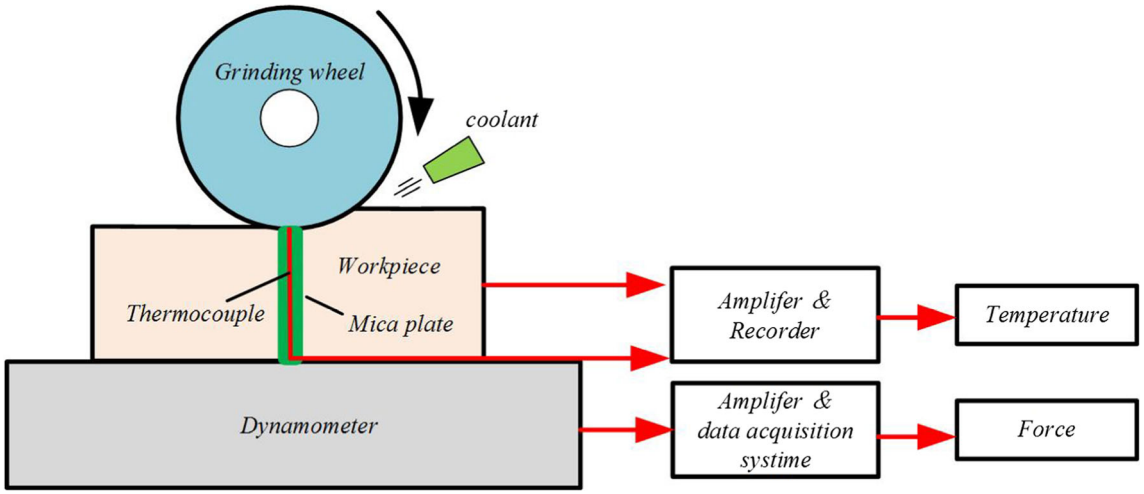

Fig. 3 The grinding temperature and force measuring diagrammatic sketch

on the surface integrity and grinding temperature, which can be expressed as [25]

$$e_s = \frac{F_t v_s}{b v_w a_p} \tag{5}$$

It is reported that the maximum undeformed chip thickness which as one of the most important parameters influenced the specific grinding energy significantly [5, 12, 26]. The maximum undeformed chip thickness was expressed as [13, 27]

$$a_{gmax} = 2(N_d C)^{-0.5} \left(\frac{v_w}{v_s}\right)^{0.5} \left(\frac{a_p}{d_s}\right)^{0.25} \tag{6}$$

where a_{gmax} is the maximum undeformed chip thickness; C is the coefficient related to the sharpness of abrasive particles; for the abrasive wheel with the abrasive grain particle size of 160–200 μm, C is chosen as 6.89 [13].

The specific grinding energy of two kinds of materials varies with the depth of cut, workpiece infeed speed, abrasive wheel speed, and maximum undeformed chip thickness as shown in Fig. 6. It can be seen that the specific grinding energy during grinding GH4169 ($e_{s\text{-}GH4169}$) superalloy material is obviously higher than that during grinding FGH96 ($e_{s\text{-}FGHs96}$) superalloy material, which indicates that the energy consumed in grinding of GH4169 superalloy material is higher than that of grinding FGH96 superalloy material. So, it can be inferred that the grinding difficulty of FGH96 superalloy material is smaller than that of GH4169 superalloy. Figure 6a shows the specific grinding energy that shows a downward trend as depth of cut increases from 0.2 to 1.5 mm in the case of $v_w = 100$ mm/min and $v_s = 25$ m/s. When $a_p = 0.2$ mm, $e_{s\text{-}GH4169} = 411.68$ J/mm^3, $e_{s\text{-}FGH96} = 315.12$ J/mm^3, while when $a_p = 1.5$ mm, $e_{s\text{-}GH4169} = 159.08$ J/mm^3, $e_{s\text{-}FGH96} = 133.23$ J/mm^3. Figure 6b shows the same trend as that of Fig. 6a. When $a_p = 0.5$ mm and $v_s = 25$ m/s, $e_{s\text{-}GH4169} = 350.77$ J/mm^3, and $e_{s\text{-}FGH96} = 268.08$ J/mm^3 at $v_w = 80$ mm/min, while $e_{s\text{-}GH4169} = 240$ J/mm^3 and $e_{s\text{-}FGH96} = 194.8$ J/mm^3 at $v_w = 150$ mm/min. From Fig. 6c, when $a_p = 0.5$ mm and $v_w = 100$ mm/min, the specific grinding energy increases with the increasing of abrasive wheel speed from 20 to 25 m/s, $e_{s\text{-}GH4169}$ from 252.93 to 297.6 J/mm^3, and $e_{s\text{-}FGH96}$ from 205.27 to 250 J/mm^3. While the specific grinding energy shows a downward trend with the increasing of abrasive wheel speed from 25 to 30 m/s, $e_{s\text{-}GH4169}$

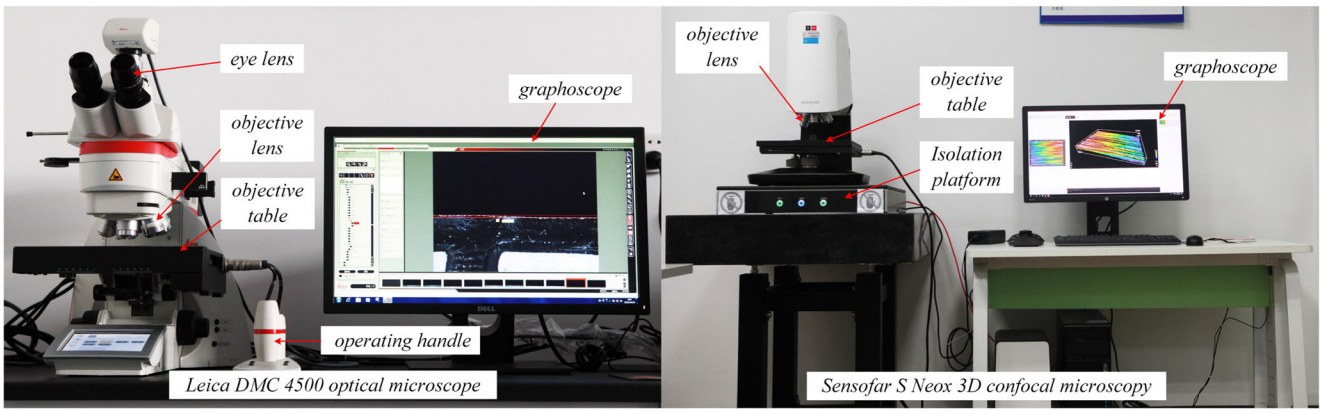

Fig. 4 Measuring device of abrasive wheel surface and ground surface

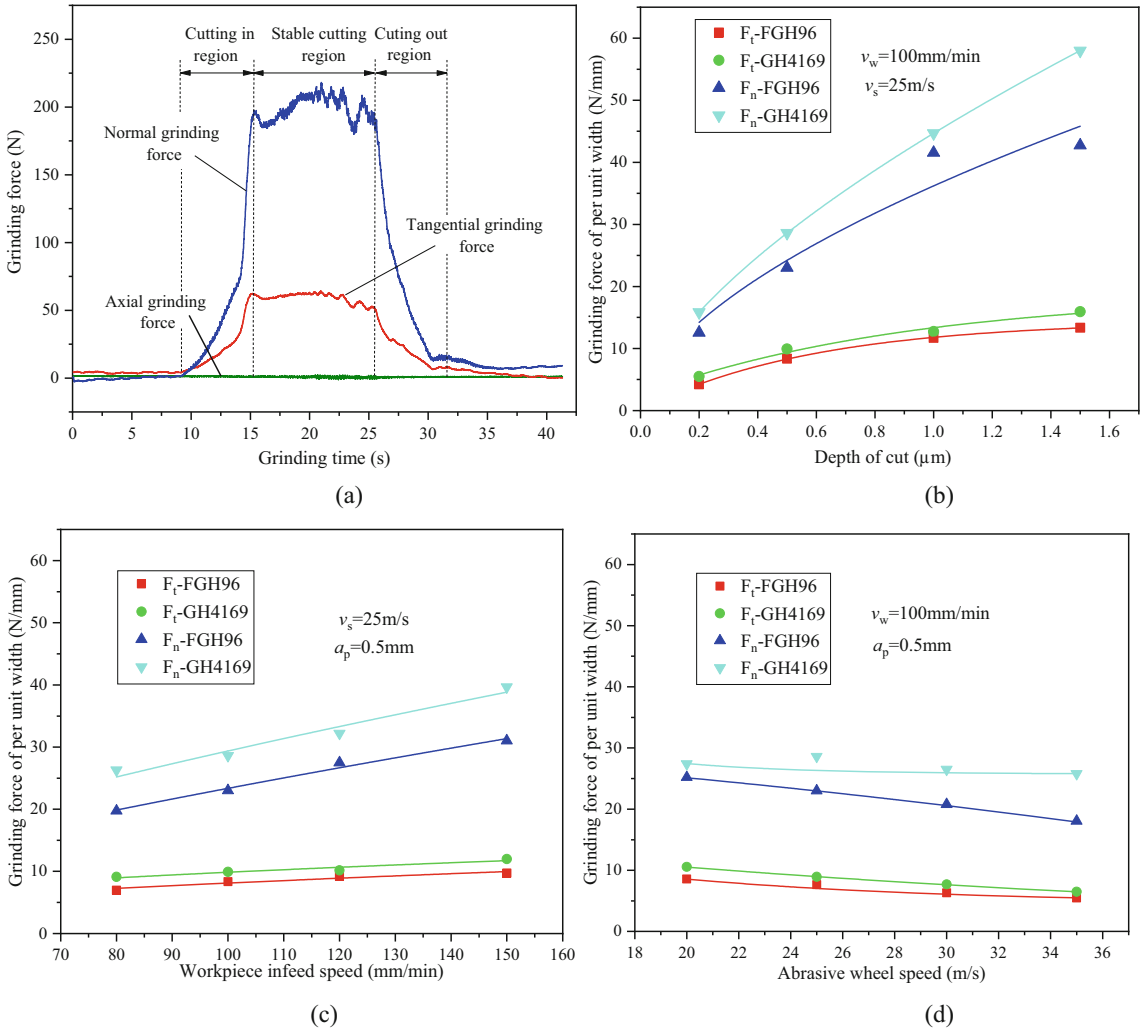

Fig. 5 Grinding force per unit width: **a** typical grinding force signal curve; and effect of **b** depth of cut, **c** workpiece infeed speed, and **d** abrasive wheel speed on grinding force

reduces to 276.65 J/mm^3, and $e_{s\text{-}FGH96}$ decreases to 226.71 J/mm^3. However, with the abrasive wheel speed increases from 30 to 35 m/s, the specific grinding energy shows an increasing trend too, $e_{s\text{-}GH4169}$ increases to 314.37 J/mm^3, while $e_{s\text{-}FGH96}$ increases to 229.29 J/mm^3. This phenomenon may be related to the "size effect" [28]. According to Fig. 6d, with the increasing of the maximum undeformed chip thickness, specific grinding energy shows a downward trend. Moreover, the specific grinding energy of GH4169 is in the range of 150 to 430 J/mm^3, while the specific grinding energy of FGH96 is in the range of 130 to 330 J/mm^3. When the maximum thickness of undeformed chip is identical, the specific grinding energy of GH4169 is larger than that of FGH96.

3.3 Analysis of grinding temperature

Grinding is the process of abrasive grain particle cutting at negative front angle, where a large amount of energy would be produced. And most of these energies are converted into heat accumulating on the workpiece surface, which results in a sharp rise in the workpiece surface temperature [29]. When the grinding temperature is too high, it would cause surface burn, residual stress, and crack of workpiece [30]. Therefore, the grinding temperature has an important effect on the machined surface integrity.

Figure 7 shows the typical grinding temperature curve and the effects of workpiece infeed speed, depth of cut, abrasive wheel speed on grinding temperature, respectively. When the abrasive wheel starts grinding the workpiece material, the grinding arc zone is far away from the measuring point, and the grinding temperature is gradually rising. This is the result of grinding heat transfer in the workpiece material. As the grinding process goes on, the grinding arc zone moves to the measuring point. The grinding temperature reaches to the highest. When the grinding arc zone is far away from the measuring point, the grinding temperature begins to decrease. And after the grinding process is finished, the surface temperature of the workpiece drops to the room temperature, as

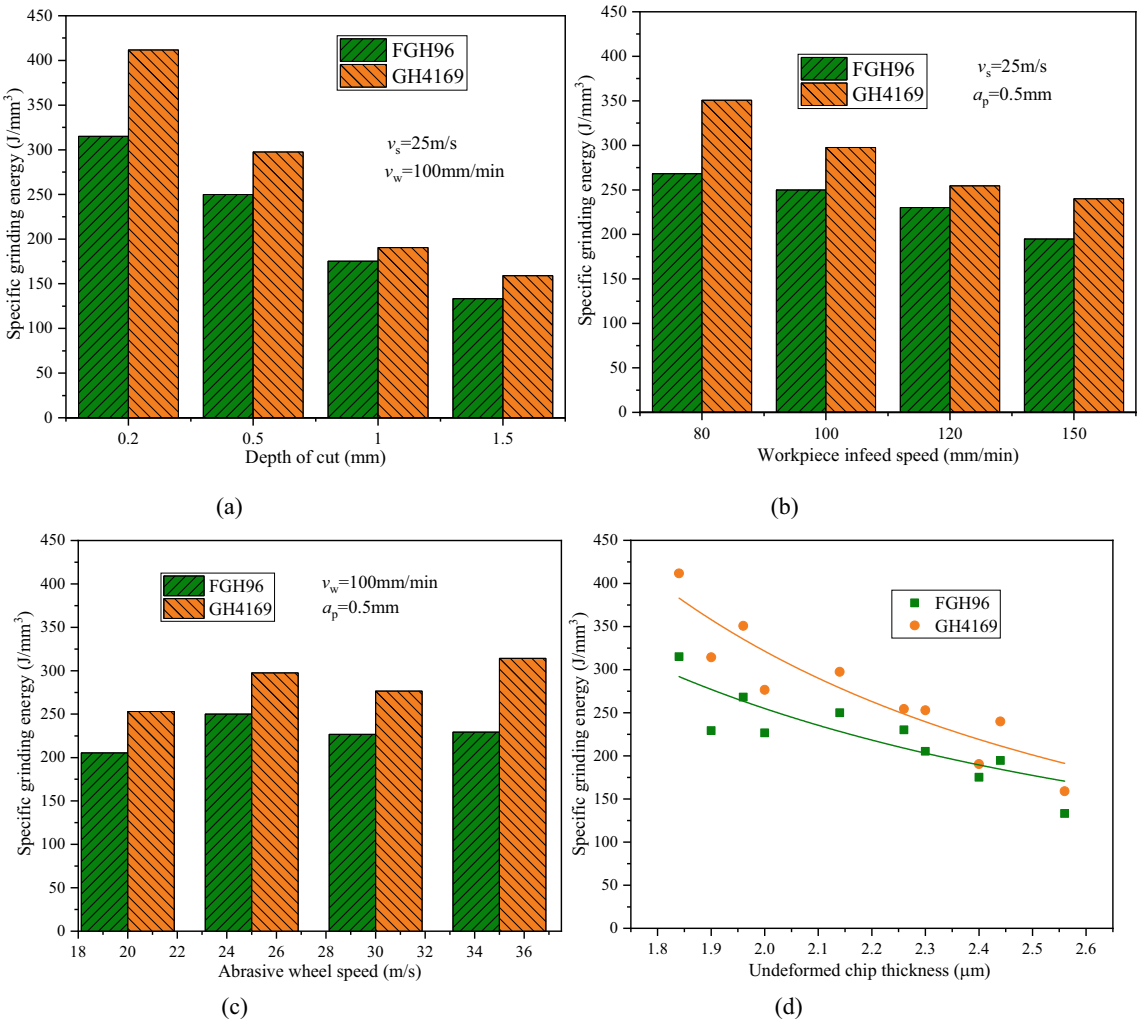

Fig. 6 Effect of **a** depth of cut, **b** workpiece infeed speed, **c** abrasive wheel speed, and **d** undeformed chip thickness on specific grinding energy

shown in Fig. 7a. It apparently found that from Fig. 7b–d, the grinding temperatures of GH4169 (T_{GH4169}) and FGH96 (T_{FGH96}) gradually increase with the increasing of workpiece infeed speed, depth of cut, and abrasive wheel speed. From Fig. 7b, when $v_w = 100$ mm/min and $v_s = 25$ m/s, with the increasing of depth of cut from 0.2 to 1.5 mm, T_{GH4169} increased by 30.2% from 725 to 944 °C, while T_{FGH96} increase by 34.2% from 588 to 789 °C. In Fig. 7c, with the workpiece infeed speed increase from 80 to 150 mm/min at $v_s = 25$ m/s and $a_p = 0.5$ mm, T_{GH4169} increases from 746 to 951 °C and increases by 27.5%; T_{FGH96} increases from 667 to 754 °C and increases by 13%. From Fig. 7d, with the increasing of abrasive wheel speed from 20 to 35 m/s at $v_w = 100$ mm/min and $a_p = 0.5$ mm, T_{GH4169} increases from 810 to 868 °C and by 7.2%; T_{FGH96} from 694 to 723 °C and by 4.2%. In addition, it can be found that the grinding temperature of GH4169 is significantly higher than that of FGH96 under the current grinding conditions. For example, at $v_w = 100$ mm/min, $v_s = 25$ m/s, and $a_p = 1$ mm, $T_{GH4169} = 900$ °C and $T_{FGH96} = 754$ °C, and the grinding temperature difference is $\triangle T = 146$ °C; at $v_w = 120$ mm/min, $v_s = 25$ m/s, and $a_p = 0.5$ mm, $T_{GH4169} = 920$ °C and $T_{FGH96} = 739$ °C, $\triangle T = 181$ °C; at $v_w = 100$ mm/min, $v_s = 30$ m/s, and $a_p = 0.5$ mm, $T_{GH4169} = 855$ °C and $T_{FGH96} = 709$ °C, $\triangle T = 146$ °C.

3.4 Simulation analysis of grinding temperature

Numerical simulation is one of the most commonly used research methods. There are several researches to use numerical methods to explore the investigated subject [29, 31–33]. In addition to directly measuring the temperature of the grinding arc zone, the grinding temperature can also be simulated and analyzed using the finite difference method. The numerical simulation principle of the finite difference method has been described in reference [33]. The heat produced in the flood grinding process is dispersed in the abrasive wheel, grinding fluid, chips, and workpiece matrix, respectively. That means that the total heat q_t consists of the following four parts: the heat transferred into the abrasive wheel q_g, the heat transferred into the grinding fluid q_f, the heat transmitted to the chips q_c,

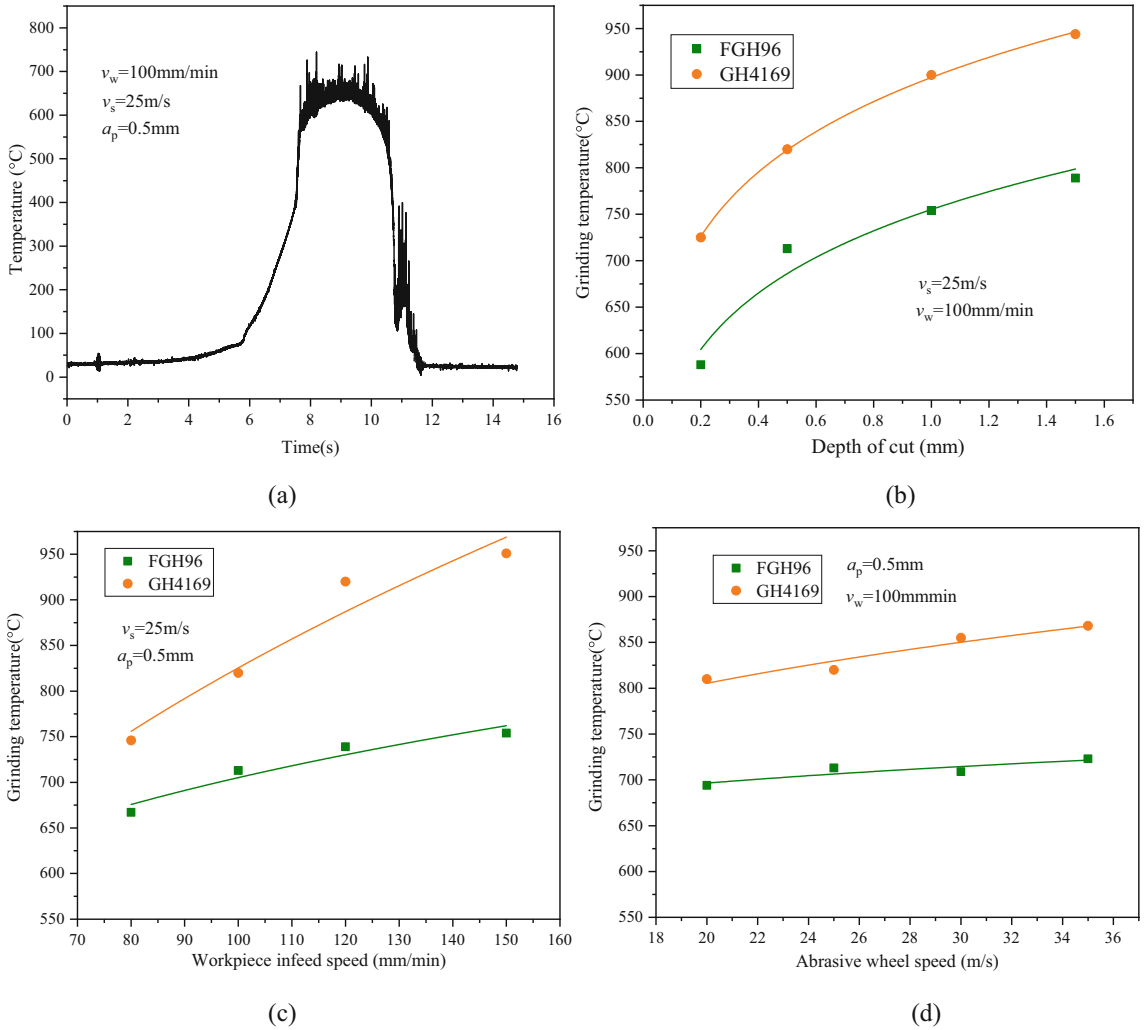

Fig. 7 Grinding temperature: **a** typical temperature signal curve during grinding, and effect of **b** depth of cut, **c** effect of workpiece infeed speed, and **d** abrasive wheel speed on grinding temperature

and the heat transferred into the workpiece q_w. The total heat q_t can be expressed as follows [33]:

$$q_t = q_g + q_f + q_c + q_w \tag{7}$$

where the heat carried away by grinding fluid and chips would not affect the ground surface of the workpiece, but the energy transferred into the workpiece is one of the most important factors affecting the surface integrity of the workpiece.

The total heat produced during the grinding process can be expressed as [30]:

$$q_t = \frac{F_t v_s}{b l_c} \tag{8}$$

Then, the heat transferred into workpiece is shown as

$$q_w = R_w q_t \tag{9}$$

where R_w is the energy ratio coefficient transferred into workpiece material, expressed as [24]

$$R_w = \frac{1}{2 + \sqrt{\frac{(\lambda\rho c)_s}{(\lambda\rho c)_w}}} \tag{10}$$

As is well known, the grinding fluid could effectively reduce the grinding temperature of the workpiece surface during the grinding process. So, the convection heat transfer of the grinding fluid cannot be ignored in the simulation work. Considering that the grinding fluid based on water-based coolant is used during the grinding process, and the jet pressure and jet velocity of the grinding fluid are very high, the convection heat transfer on the workpiece surface outside the grinding arc zone obtained by calculating is turbulent forced convection heat transfer. However, the boiling heat transfer occurs because of the high grinding temperature at the grinding arc zone. So, the convection heat transfer mode of the grinding fluid in the grinding arc zone is boiling heat transfer. Therefore, the heat transfer coefficient of grinding fluid

consists of turbulent forced convection heat transfer coefficient and boiling heat transfer coefficient.

The turbulent forced convection heat transfer coefficient can be expressed as [34]

$$h_f = \frac{k_l N_u}{b} \tag{11}$$

where N_u is the Nussel number

$$N_u = 0.037 R_e^{4/5} {P_{rl}}^{1/3} \tag{12}$$

where R_e is the Reynolds number

$$R_e = \nu_l l_w / \mu_l \tag{13}$$

The boiling heat transfer coefficient would be shown as [35]

$$h = K \left[\frac{L_l g \rho_v k_v^3 (\rho_l - \rho_v)}{\sqrt{\frac{8\sigma T_{sat} q_l}{\rho_v L_l k_l}} \mu_l l_c} \right]^{0.25} \tag{14}$$

where h is the heat transfer coefficient of grinding fluid W/(m^2 · K), K is the constant, g is the acceleration of gravity (m/s^2), q_l is the heat flux of grinding fluid (W/m^2), L_l is the latent heat of vaporization of grinding fluid (J/kg), P_{rl} is the Trump number, v_l is the jet velocity of grinding fluid (m/s), l_w is the workpiece length (m), l_c is the grinding arc length (m), ρ_l is the density of grinding fluid (kg/m^3), ρ_v is the density of steam (kg/m^3), k_l is the thermal conductivity of grinding fluid W/(m · K), k_v is the thermal conductivity of steam W/(m · K), μ_l is the dynamic viscosity of grinding fluid (m^2/s), σ is the surface tension of grinding fluid (N/m), T_{sat} is the saturation temperature of grinding fluid (°C), σ is the surface tension of grinding fluid (N/m).

In the process of flood grinding, in order to calculate each parameter value of grinding fluid conveniently, it can be replaced by the parameter value of water. It is necessary to note that firstly, the grinding arc zone is the wedge area formed by the abrasive wheel and the workpiece material. In this wedge region, it can be considered that the heat flux density of grinding fluid is the same as that of workpiece surface, that is, $q_l = q_w$; secondly, due to the high jet pressure and velocity of grinding fluid, the convection heat transfer coefficient is much higher than that of air. Therefore, the convection heat transfer coefficient of air is neglected in the simulation work.

As shown in Fig. 8, the grinding heat distribution of FGH96 and GH4169 is obtained by MATLAB finite difference simulation at $v_w = 100$ mm/min, $v_s = 25$ m/s, and $a_p = 0.5$ mm, respectively. The simulation results agree with the results in Fig. 7 that the grinding temperature of GH4169 is higher than that of FGH96. It has two main reasons on this result: on one hand, the grinding force and specific grinding energy obtained by grinding GH4169 are higher than those of FGH96, so the heat flux is higher than FGH96, which leads to the grinding temperature being higher; on the other hand, it can be seen from Table 2 that the heat transfer coefficient of GH4169 is higher than that of FGH96 superalloy material. Then, the heat transferred into GH4169 workpiece surface is more than that of FGH96 workpiece during grinding. Therefore, the magnitude of heat transfer coefficient is also one of the important factors affecting grinding temperature.

3.5 Analysis of abrasive wheel wear

The abrasive wheel wear behavior is another important parameter to evaluate the grinding characteristics of materials, which has an extremely important influence on the surface integrity of workpiece. In this article, only the wear behavior of abrasive wheel in stable grinding stage is studied. The radial wear of abrasive wheel is the most direct parameter to evaluate the wear degree of abrasive wheel. In the experiment, the abrasive wheel surface can be compounded by grinding blade which made by stainless steel with the thickness is 0.02 mm. The wear of the abrasive wheel is indirectly measured by measuring the height difference between the unworn surface and the worn surface on the blade, shown in Fig. 9a. As shown in Fig. 9b–d, the radial wear of abrasive wheel varies with grinding parameters. It can be found that the abrasive wheel wear of two kinds of superalloy materials varies greatly with the change of grinding parameters, which indicates that the abrasive wheel wear is serious in the process of grinding these two Ni-based superalloys. Seen from Fig. 9b, the radial wear of abrasive wheel increases with increasing of depth of cut. Radial wear of abrasive wheel when grinding FGH96 ($W_{R\text{-}FGH96}$) increases linearly, while the radial wear of abrasive wheel when grinding GH4169 ($W_{R\text{-}GH4169}$) is increasing slowly, when the depth of cut increases from 0.2 to 1.5 mm. In addition, in case of $a_p < 0.8$ mm, $W_{R\text{-}GH4169}$ is higher than $W_{R\text{-}FGH96}$ with the increase of depth of cut. For instance, at $a_p = 0.5$ mm, $R_{GH4169} = 0.34$ μm/mm, $W_{R\text{-}FGH96} = 0.29$ μm/mm; when $a_p > 0.8$ mm, $W_{R\text{-}GH4169}$ is less than $W_{R\text{-}FGH96}$ with the increase of depth of cut. For instance, at $a_p = 1$ mm, $W_{R\text{-}FGH96} = 0.4$ μm/mm, $W_{R\text{-}GH4169} = 0.36$ μm/mm. Seen from Fig. 9c, at $a_p = 0.5$ mm and $v_s = 25$ m/s, when the workpiece infeed speed increases from 80 to 100 mm/min and from 120 to 150 mm/min, the radial wear of abrasive wheel decreases with the increasing of workpiece infeed speed. When the workpiece infeed speed increases from 100 to 120 mm/min, the radial wear of abrasive wheel increases with the increasing of workpiece infeed speed. The decrease-increase-decrease trend may be related with the grain damage of abrasive wheel surface after dressing. But the mechanism of abrasive wheel wear should be deeper studied. In addition, when $v_w < 108$ mm/min, $W_{R\text{-}GH4169}$ is higher than $W_{R\text{-}FGH96}$, for example, at $v_w = 80$ mm/min, $W_{R\text{-}GH4169} = 0.4$ μm/mm, and $W_{R\text{-}FGH96} = 0.34$ μm/mm; when $v_w > 108$ mm/min, $W_{R\text{-}GH4169}$ is

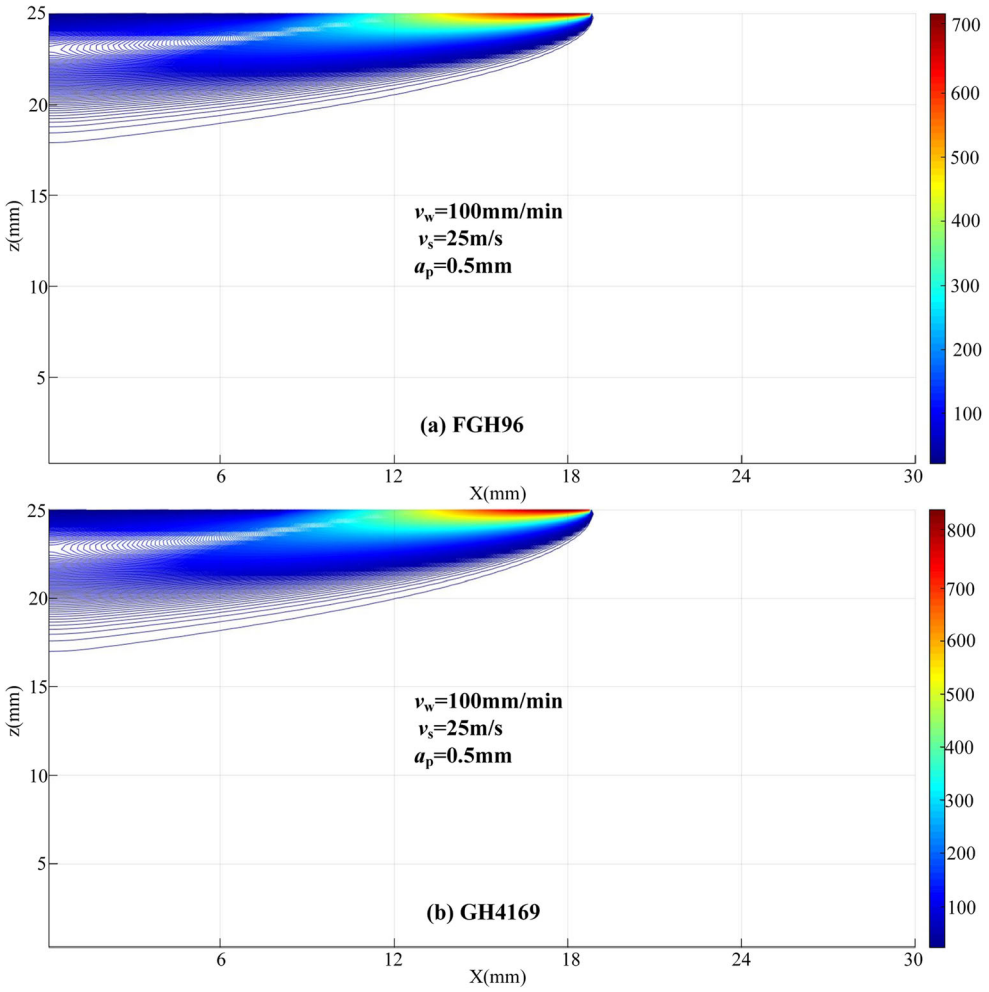

Fig. 8 Simulated grinding temperature fields of **a** FGH96 and **b** GH4169

less than $W_{R\text{-}FGH96}$, for example, at $v_w = 120$ mm/min, $W_{R\text{-}GH4169} = 0.37$ μm/mm, and $W_{R\text{-}FGH96} = 0.44$ μm/mm. From Fig. 9d, at $v_w = 100$ mm/min and $a_p = 0.5$ mm, $W_{R\text{-}GH4169}$ shows a trend of firstly increasing and then decreasing and then increasing, while $W_{R\text{-}FGH96}$ gives a trend of decreasing first and then increasing.

Figure 10 shows the surface morphology of the abrasive wheel after grinding different superalloy materials in case of $v_w = 100$ mm/min, $v_s = 25$ m/s, and $a_p = 1$ mm. Generally, there is no serious adhesion or hole plugging on the surface of the abrasive wheel after grinding FGH96 and GH4169 superalloy materials. However, according to the experimental results of the radial wear of the abrasive wheel, under the same grinding conditions, the abrasive wheel wear produced in grinding FGH96 and GH4169 superalloy material is basically the same, which shows that the grinding performance of the brown corundum abrasive wheel used in the experiment is similar to that of the two kinds of superalloy materials. What is more, the wear degree difference of abrasive wheel between the two kinds of superalloy materials is not obvious. On one hand, the grinding force of FGH96 is slightly smaller than that of GH4169; then, the effect of grinding force on the difference of abrasive wheel wear for these two materials can be neglected. On the other hand, although the temperature of FGH96 is smaller than that of GH4169, it should not ignore the fact that the mechanical strength of FGH96 superalloy material is higher than that of GH4169 superalloy material at elevated temperature, as listed in Table 2, which results in a higher wear rate of abrasive wheel.

3.6 Sensitive analysis of ground surface roughness

Ground surface roughness, which has an important effect on fatigue life and durability of workpiece, is also an important parameter to reflect the surface integrity of workpiece [36]. Figure 11 is a sampling diagram for surface roughness of two kinds of workpiece materials ground at $v_w = 100$ mm/min, $v_s = 25$ m/s, and $a_p = 1.5$ mm. The sampling method is to measure the roughness of multiple positions in the vertical grinding direction and calculating the average value. As can be seen from Fig. 11, when the depth of cut is 1.5 mm, the height of surface grooves of two kinds of superalloy materials are very high. The values of the height values of grooves on ground surface of FGH96 workpiece range from − 3.3 to 2.2 μm,

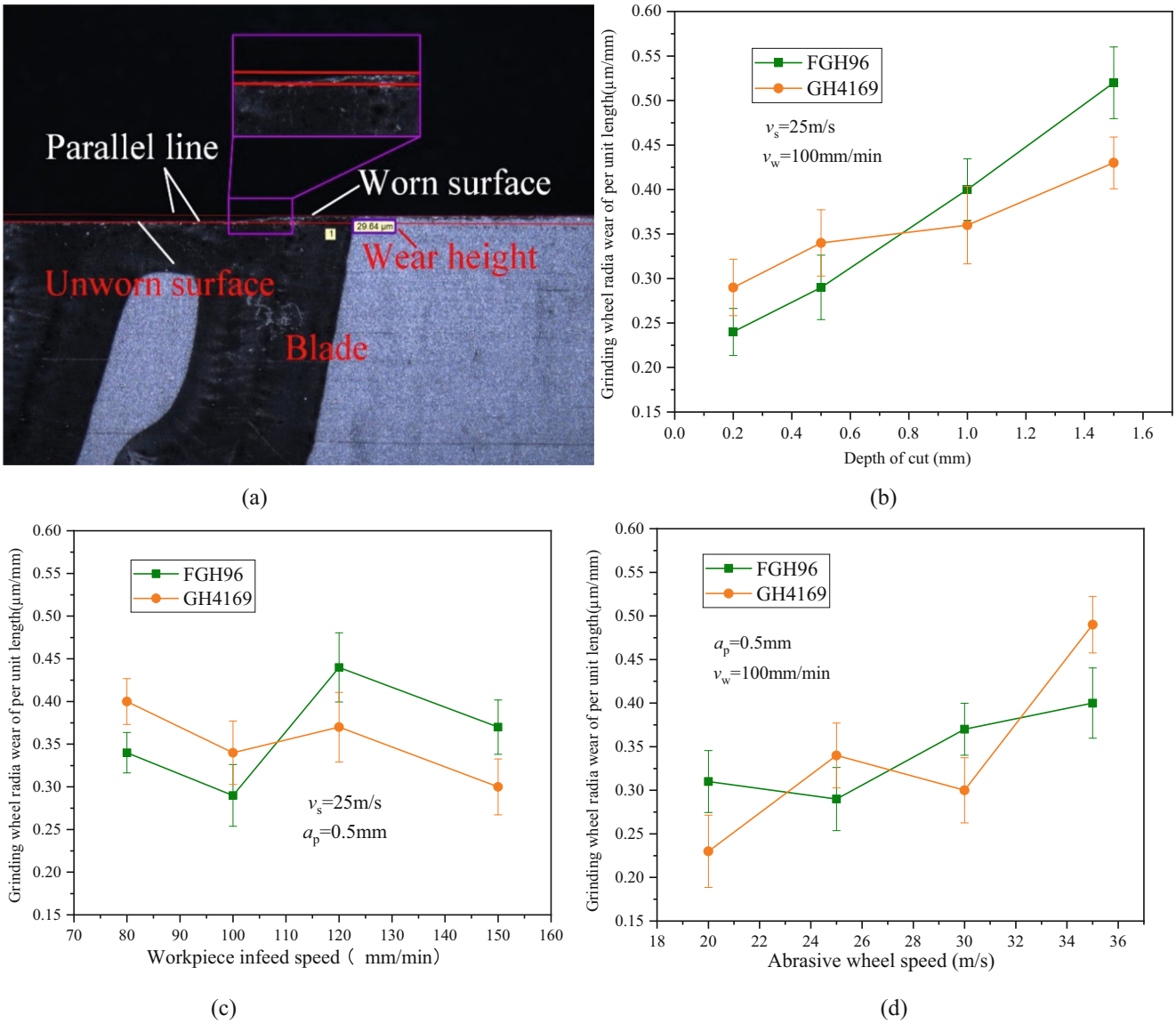

Fig. 9 Radial wear of abrasive wheel: **a** abrasive wheel radial wear schematic diagram and effect of **b** depth of cut, **c** workpiece infeed speed, and **d** abrasive wheel speed on abrasive wheel radial wear of per unit length

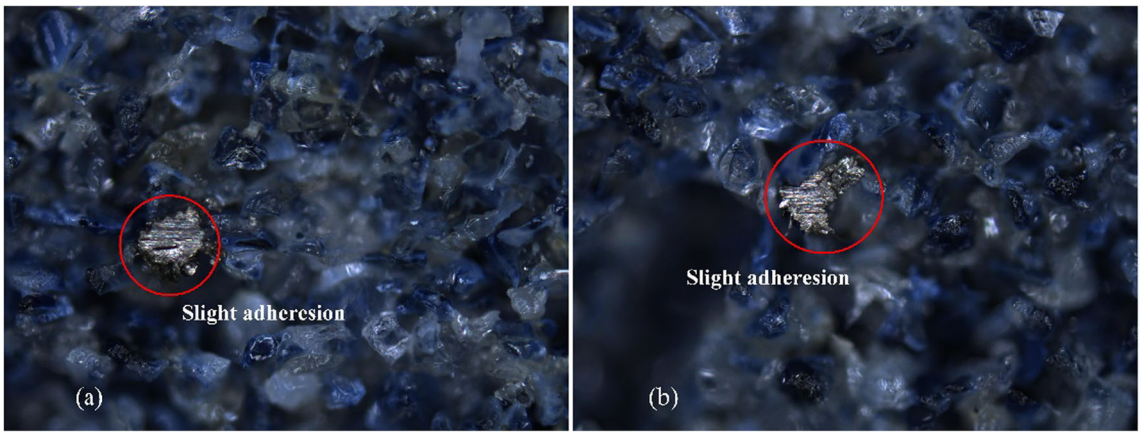

Fig. 10 Surface morphology of abrasive wheel after grinding **a** FGH96 and **b** GH4169 superalloy materials

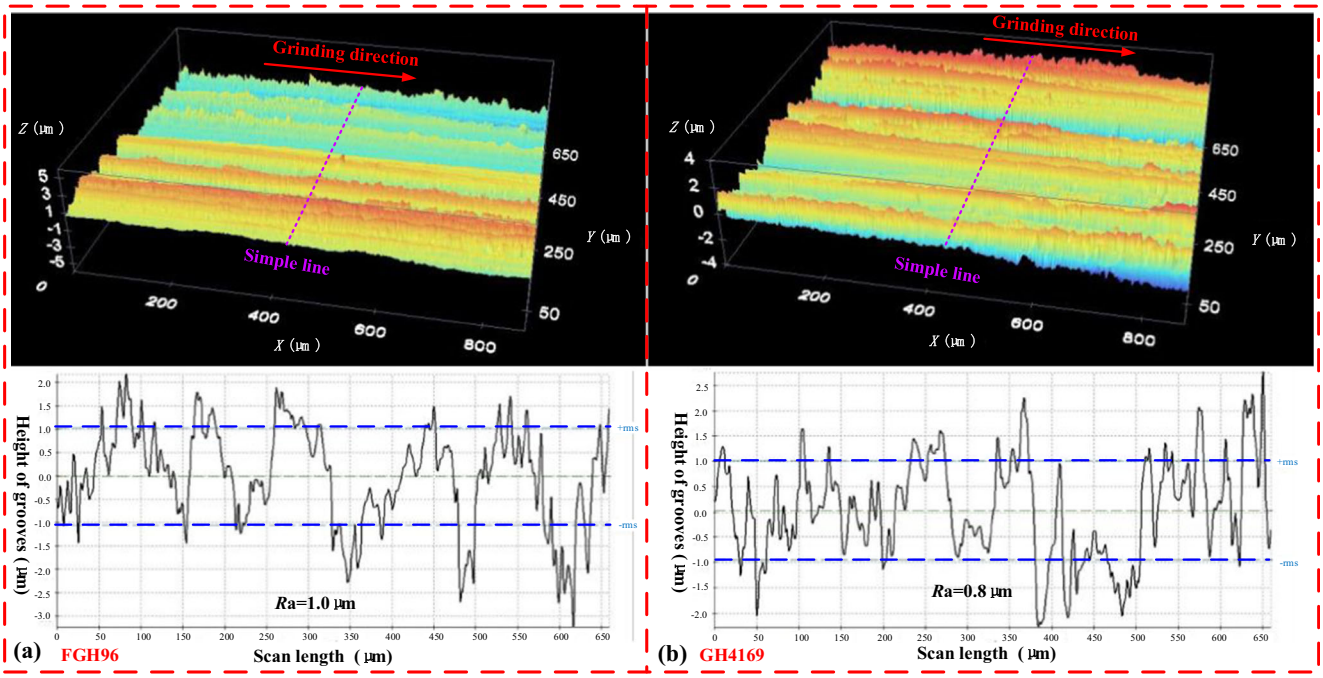

Fig. 11 Surface roughness sampling schematic diagram of **a** FGH96 and **b** GH4169 superalloy materials

while for GH4169 workpiece, the height values range from − 2.4 to 2.8 μm. This indicated that the surface roughness values of both materials are relatively large.

The ground surface roughness values of FGH96 and GH4169 are shown in Fig. 12. From Fig. 12a, when v_w = 100 mm/min and v_s = 25 m/s, the ground surface roughness values of FGH96 ($R_{a\text{-FGH96}}$) and GH4169 ($R_{a\text{-GH4169}}$) increase with the increase of depth of cut. $R_{a\text{-FGH96}}$ increases from 0.28 to 0.99 μm, increasing by 254%, while $R_{a\text{-GH4169}}$ increases from 0.42 to 0.79 μm, increasing by 88.1%, which shows that the influence of depth of cut on ground surface roughness of FGH96 workpiece is greater than that on GH4169. In addition, when $a_p < 0.55$ mm, $R_{a\text{-GH4169}} > R_{a\text{-FGH96}}$, while when $a_p > 0.55$ mm, $R_{a\text{-GH4169}} < R_{a\text{-FGH96}}$. This may be because the wear rate of abrasive wheel in grinding FGH96 is higher than that in grinding GH4169 when $a_p < 0.55$ mm. From Fig. 12b, $R_{a\text{-FGH96}}$ increases from 0.51 to 0.87 μm increasing by 70.6%, while $R_{a\text{-GH4169}}$ increases from 0.45 to 0.66 μm increasing by 46.7% at v_s = 25 m/s and a_p = 0.5 mm with the workpiece infeed speed increase from 80 mm/min to 150 mm/min. From Fig. 12c, the surface roughness of those two kinds of superalloy materials shows a tendency of decreasing firstly and then increasing with the abrasive wheel speed increasing from 20 to 35 m/s when v_w = 100 mm/min and a_p = 0.5 mm. At v_s = 30 m/s, the minimum values of ground surface roughness are obtained, $R_{a\text{-FGH96}}$ = 0.47 μm and $R_{a\text{-GH4169}}$ = 0.45 μm, respectively.

The ground surface roughness mainly depends on the appearance height of abrasive grains on the surface of abrasive wheel. When the extruding height of abrasive grains is higher, that is when the actual cutting depth of abrasive grains is larger, the surface grooves of ground workpieces are deeper, then the surface roughness value is relatively larger [5, 37, 38]. It should be noted that the actual cutting depth of the abrasive grains is related to the grinding parameters under the identical tool conditions and the identical dressing parameters. So, the ground surface roughness can be expressed by the grinding parameters.

The relationship between ground surface roughness and grinding parameters by least square fitting can be expressed as follows:

$$\text{For FGH96}: R_a = 2.36 a_p^{0.586} v_w^{0.32} v_s^{-0.554} \quad (15)$$

$$\text{For GH4169}: R_a = 11.1 a_p^{0.329} v_w^{0.751} v_s^{-0.982} \quad (16)$$

Where the average error value of formula (15) is 6.1%, while the average error value of formula (16) is 4.9%. As is well known, the surface state of abrasive wheel and grinding conditions has a great effect on the ground surface roughness. It notes that the fitting eq. (13) and (14) are merely the relationship between surface roughness Ra and grinding parameters, while it does not consider the effect of surface state of abrasive wheel and other factors on ground surface roughness.

From eq. (15) and (16), it can be found that the grinding surface roughness is positively correlated with workpiece infeed speed and depth of cut, while it is negatively correlated with abrasive wheel speed at the same surface state of abrasive wheel and cooling conditions. However, the sensitivity of surface roughness to the variation of grinding parameters cannot be obtained from formulas (15) and (16). By analyzing the

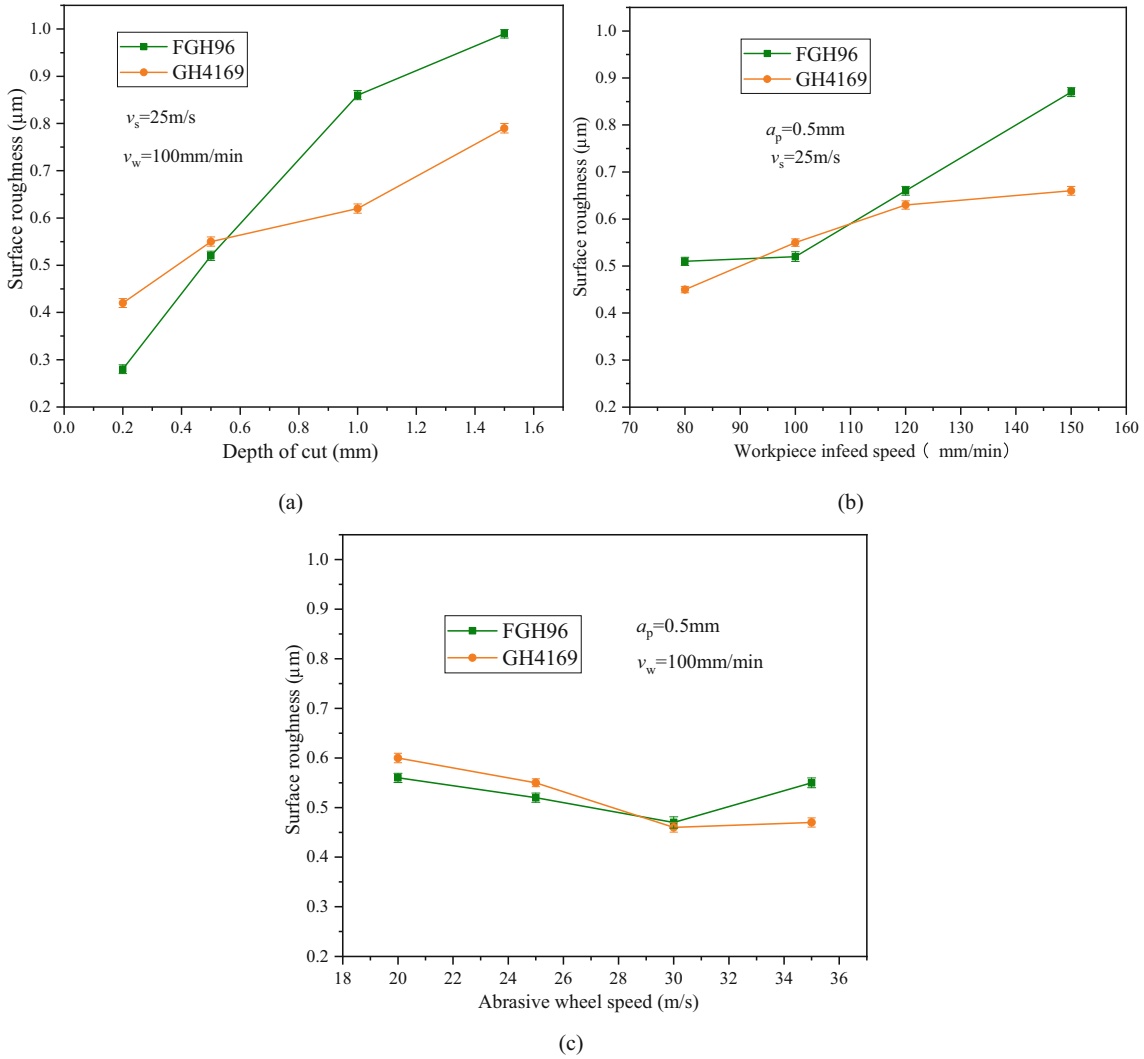

Fig. 12 Effect of **a** depth of cut, **b** workpiece infeed speed, and **c** abrasive wheel speed on ground surface roughness

sensitivity of surface integrity in milling process, ideal conclusions were obtained in Ref. [39, 40]. Therefore, the sensitivity analysis method was used to achieve the sensitivity of surface roughness produced in grinding GH4169 and

Table 4 Calculation results of absolute sensitivity of ground surface roughness to grinding parameters of GH4169 and FGH96

	v_s (m/s)	v_w (mm/s)	a_p (mm)	$\frac{\partial R_a}{\partial a_p}$	$\frac{\partial R_a}{\partial v_w}$	$\left\lvert\frac{\partial R_a}{\partial v_s}\right\rvert$
FGH96	25	100	1	0.46	0.62	0.017
	25	100	0.2	0.89	0.24	0.007
	20	100	0.5	0.69	0.47	0.016
	35	100	0.5	0.51	0.34	0.007
	25	80	0.5	0.44	0.38	0.008
	25	150	0.5	1.04	0.47	0.02
GH4169	25	100	1	0.23	0.4	0.027
	25	100	0.2	0.67	0.24	0.016
	20	100	0.5	0.45	0.4	0.034
	35	100	0.5	0.26	0.23	0.011
	25	80	0.5	0.3	0.3	0.018
	25	150	0.5	0.49	0.35	0.029

FGH96 to different grinding parameters under the current experimental conditions.

The absolute sensitivity of ground surface roughness to depth of cut, workpiece infeed speed, and abrasive wheel speed for GH4169 and FGH96 is calculated as follows:

For depth of cut

$$: \begin{cases} \dfrac{\partial R_{\mathrm{a-GH4169}}}{\partial a_{\mathrm{p}}} = 1.38 a_{\mathrm{p}}^{-0.414} v_{\mathrm{w}}^{1.32} v_{\mathrm{s}}^{-0.554} \\ \dfrac{\partial R_{\mathrm{a-FGH96}}}{\partial a_{\mathrm{p}}} = 3.65 a_{\mathrm{p}}^{-0.671} v_{\mathrm{w}}^{0.751} v_{\mathrm{s}}^{-0.982} \end{cases} \tag{17}$$

For workpiece infeed speed

$$: \begin{cases} \dfrac{\partial R_{\mathrm{a-GH4169}}}{\partial v_{\mathrm{w}}} = 3.12 a_{\mathrm{p}}^{0.586} v_{\mathrm{w}}^{0.322} v_{\mathrm{s}}^{-0.554} \\ \dfrac{\partial R_{\mathrm{a-FGH96}}}{\partial v_{\mathrm{w}}} = 8.33 a_{\mathrm{p}}^{0.329} v_{\mathrm{w}}^{0.249} v_{\mathrm{s}}^{-0.982} \end{cases} \tag{18}$$

For abrasive wheel speed

$$: \begin{cases} \left| \dfrac{\partial R_{\mathrm{a-GH4169}}}{\partial v_{\mathrm{s}}} \right| = 1.31 a_{\mathrm{p}}^{0.586} v_{\mathrm{w}}^{1.32} v_{\mathrm{s}}^{-1.55} \\ \left| \dfrac{\partial R_{\mathrm{a-FGH96}}}{\partial v_{\mathrm{s}}} \right| = 8.33 a_{\mathrm{p}}^{0.329} v_{\mathrm{w}}^{0.249} v_{\mathrm{s}}^{-0.982} \end{cases} \tag{19}$$

Table 4 lists the results of the absolute sensitivity analysis of the ground surface roughness of GH4169 and FGH96 to the depth of cut, workpiece infeed speed, and the abrasive wheel speed. It is found that the sensitivity of ground surface roughness of FGH96 superalloy material to the depth of cut and workpiece infeed speed is greater than that of GH4169 superalloy material. The sensitivity of ground surface roughness of FGH96 superalloy material to the abrasive wheel speed is less than that of GH4169 superalloy material, which is also consistent with the surface roughness results of the two kinds of superalloy materials. The surface roughness of the two kinds of superalloy materials is the most sensitive to depth of cut, followed by workpiece infeed speed, and the least sensitive to the abrasive wheel speed through the comprehensive comparison analysis. When the abrasive wheel speed and workpiece infeed speed are the same, the sensitivity of ground surface roughness to depth of cut decreases with the increase of depth of cut. For example, as for FGH96, when $v_{\mathrm{w}} = 100$ mm/min and $v_{\mathrm{s}} = 25$ m/s, $\frac{\partial R_a}{\partial R_p} = 0.89$ at $a_{\mathrm{p}} = 0.2$ mm, while $\frac{\partial R_a}{\partial a_p} = 0.46$ at $a_{\mathrm{p}} = 1$ mm. When the depth of cut and abrasive wheel speed are the same, the sensitivity of ground surface roughness to workpiece infeed speed increases with the increase of workpiece infeed speed. For example, as for FGH96, when $v_{\mathrm{s}} = 25$ m/s and $a_{\mathrm{p}} = 0.5$ mm, $\frac{\partial R_a}{\partial v_w} = 0.38$ at $v_{\mathrm{w}} = 80$ mm/min, while $\frac{\partial R_a}{\partial v_w} = 0.47$ at $v_{\mathrm{w}} = 150$ mm/min. When the workpiece infeed speed and depth of cut are identical, the sensitivity of ground surface roughness to abrasive wheel speed increases with the increase of abrasive wheel speed. For instance, as for FGH96, when $v_{\mathrm{w}} = 100$ mm/s and $a_{\mathrm{p}} = 0.5$ mm, $\left|\frac{\partial R_a}{\partial v_s}\right| = 0.016$ at $v_{\mathrm{s}} = 20$ m/s, while $\left|\frac{\partial R_a}{\partial v_s}\right| = 0.007$ at $v_{\mathrm{s}} = 35$ m/s.

4 Conclusion

(1) The grinding force, grinding temperature, and specific grinding energy of GH4169 superalloy material are generally higher than those of FGH96 superalloy material, and the abrasive wheel wear pattern in grinding GH4169 and FGH96 is generally the same under the given experimental conditions.

(2) The surface roughness of both the two kinds of nickel-base superalloy materials is the most sensitive to depth of cut, followed by workpiece infeed speed, and the least sensitive to the abrasive wheel speed. Furthermore, the sensitivity of ground surface roughness of FGH96 superalloy material to the depth of cut and workpiece infeed speed is greater than that of GH4169. The sensitivity of ground surface roughness of FGH96 to the abrasive wheel speed is less than that of GH4169.

(3) Based on the comprehensive analysis, the machinability of FGH96 is slightly better than that of GH4169 under the identical grinding experimental conditions.

Funding information This work was financially supported by the National Natural Science Foundation of China (No. 51775275), the Fundamental Research Funds for the Central Universities (No. NE2014103).

References

1. Ding WF, Xu JH, Cheng ZZ, Fu YC (2010) Grindability and surface integrity of cast nickel-base superalloy in creep feed grinding with brazed CBN abrasive wheels. Chin J Aeronaut 23:501–510
2. Devillez A, Coz GL, Dominiak S, Dudzinski D (2011) Dry machining of Inconel 718 workpiece surface integrity. J Mater Process Technol 211:1590–1598
3. Pusavec F, Deshpande A, Yang S, M'Saoubi R, Kopac J, Dillon OW Jr, Jawahir IS (2014) Sustainable machining of high temperature nickel alloy - Inconel 718: part 1 - predictive performance models. J Clean Prod 81:255–269
4. Wang YG, Li CH, Zhang YB, Yang M, Zhang XP, Zhang NQ, Dai JJ (2017) Experimental evaluation on tribological performance of the wheel/workpiece interface in minimum quantity lubrication grinding with different concentrations of Al_2O_3 nanofluids. J Clean Prod 142:3571–3583
5. Dai CW, Ding WF, Zhu YJ, Xu JH, Yu HW (2018) Grinding temperature and power consumption in high speed grinding of Inconel 718 nickel-base superalloy with a vitrified CBN wheel. Precis Eng 52:192–200
6. Dudzinski D, Devillez A, Moufki A, Larrouquere D, Zerrouki V, Vigneau J (2004) A review of developments towards dry and high

speed machining of Inconel 718 alloy. Int J Mach Tools Manuf 44: 439–456
7. Bhatt A, Attia H, Vargas R, Thomson V (2010) Wear mechanisms of WC coated and uncoated tools in finish turning of Inconel 718. Tribol Int 43:1113–1121
8. Sugihara T, Takemura S, Enomoto T (2016) Study on high-speed machining of Inconel 718 focusing on tool surface topography of CBN cutting tool. Int J Adv Manuf Technol 87:9–17
9. Du J, Liu ZQ (2013) Damage of the machined surface and subsurface in orthogonal milling of FGH95 superalloy. Int J Adv Manuf Technol 68:1573–1581
10. Du J, Liu ZQ, Yi W, Su G (2011) Influence of cutting speed on surface integrity for powder metallurgy nickel-base superalloy FGH95. Int J Adv Manuf Technol 56:553–559
11. Du J, Liu ZQ (2012) Effect of cutting speed on surface integrity and chip morphology in high-speed machining of PM nickel-base superalloy FGH95. Int J Adv Manuf Technol 60:893–899
12. Huddedar S, Chitalkar P, Chavan A, Pawade RS (2012) Effect of cooling environment on grinding performance of nickel based superalloy Inconel 718. J Appl Sci 12:947–954
13. Qian N, Ding W, Zhu Y (2018) Comparative investigation on grindability of K4125 and Inconel718 nickel-base superalloys. Int J Adv Manuf Technol 97:1649–1661
14. Xi XX, Ding WF, Fu YC, Xu JH (2018) Grindability evaluation and tool wear during grinding of Ti_2AlNb intermetallics. Int J Adv Manuf Technol 94:1441–1450
15. Balan ASS, Vijayaraghavan L, Krishnamurthy R, Kuppan P, Oyyaravelu R (2016) An experimental assessment on the performance of different lubrication techniques in grinding of Inconel 751. J Adv Res 7:709–718
16. Jia DZ, Li CH, Zhang YB, Yang M, Wang YG, Guo SM, Cao HJ (2017) Specific energy and surface roughness of minimum quantity lubrication grinding Ni-based alloy with mixed vegetable oil-based nanofluids. Precis Eng 50:248–262
17. Guo SM, Li CH, Zhang YB, Wang YG, Li BK, Yang M, Zhang XP, Liu GT (2017) Experimental evaluation of the lubrication performance of mixtures of castor oil with other vegetable oils in MQL grinding of nickel-base alloy. J Clean Prod 140:1060–1076
18. Li S, Wu Y, Nomura M (2016) Effect of abrasive wheel ultrasonic vibration on chip formation in surface grinding of Inconel 718. Int J Adv Manuf Technol 86:1113–1125
19. Yao CF, Jin QC, Huang XC, Wu DX, Ren JX, Zhang DH (2013) Research on surface integrity of grinding Inconel718. Int J Adv Manuf Technol 65:1019–1030
20. Hecker RL, Liang SY (2003) Predictive modeling of surface roughness in grinding. Int J Mach Tools Manuf 43:755–761
21. Ding WF, Dai CW, Yu TY, Xu JH, Fu YC (2017) Grinding performance of textured monolayer CBN wheels: Undeformed chip thickness nonuniformity modeling and ground surface topography prediction. Int J Mach Tools Manuf 122:66–80
22. Zhang MJ, Li FG, Wang SY (2011) Effect of powder preparation technology on the hot deformation behavior of HIPed P/M nickel-base superalloy FGH96. Mater Sci Eng A 528:4030–4039
23. Peng Z, Tian GF, Jiang J, Li MZ, Chen Y, Zou JW, Dunne FP (2016) Mechanistic behaviour and modelling of creep in powder metallurgy FGH96 nickel superalloy. Mater Sci Eng A 676:441–449
24. Malkin S, Guo C (2008) Grinding technology: theory and applications of machining with abrasives, 2nd edn. Industrial Press, New York
25. Chen JY, Huang H, Xu XP (2010) Grinding characteristics in high speed grinding of engineering ceramics with brazed diamond wheels. J Mater Process Technol 210:899–906
26. Yang M, Li CH, Zhang YB, Jia DZ, Zhang XP, Hou YL, Li RZ, Wang J (2017) Maximum undeformed equivalent chip thickness for ductile-brittle transition of zirconia ceramics under different lubrication conditions. Int J Mach Tools Manuf 122:55–65
27. Tang J, Du J, Chen Y (2009) Modeling and experimental study of grinding forces in surface grinding. J Mater Process Technol 209: 2847–2854
28. Heinzel C, Bleil N (2007) The use of the size effect in grinding for work-hardening. CIRP Ann Manuf Technol 56:327–330
29. Zhang JC, Li CH, Zhang YB, Yang M, Jia DZ, Hou YL, Li RZ (2018) Temperature field model and experimental verification on cryogenic air nanofluid minimum quantity lubrication grinding. Int J Adv Manuf Technol 96:1–20
30. Yin GX, Marinescu ID (2017) A heat transfer model of grinding process based on energy partition analysis and grinding fluid cooling application. J Manuf Sci Eng 139:121015
31. Qi H, Wen DH, Yuan QL, Zhang L, Chen ZZ (2017) Numerical investigation on particle impact erosion in ultrasonic-assisted abrasive slurry jet micro-machining of glasses. Powder Technol 314: 627–634
32. Qi H, Wen DH, Lu CD, Li G (2016) Numerical and experimental study on ultrasonic vibration-assisted micro-channelling of glasses using an abrasive slurry jet. Int J Mech Sci 110:94–107
33. Yang M, Li CH, Zhang YB, Jia DZ, Zhang XP, Hou YL, Shen B, Li RZ (2018) Microscale bone grinding temperature by dynamic heat flux in nanoparticle jet mist cooling with different particle sizes. Mater Manuf Process 33:58–68
34. Mao C, Zou H, Huang Y, Li Y, Zhou ZX (2013) Analysis of heat transfer coefficient on workpiece surface during minimum quantity lubricant grinding. Int J Adv Manuf Technol 66:363–370
35. Mohanta L, Sohag FA, Cheung FB, Bajorek SM, Kelly JM, Tien K, Hoxie CL (2017) Heat transfer correlation for film boiling in vertical upward flow. Int J Heat Mass Transf 107:112–122
36. Yao CF, Tan L, Yang P, Zhang DH (2018) Effects of tool orientation and surface curvature on surface integrity in ball end milling of TC17. Int J Adv Manuf Technol 94:1699–1710
37. Ulutan D, Ozel T (2011) Machining induced surface integrity in titanium and nickel alloys: a review. Int J Mach Tools Manuf 51: 250–280
38. Rabiei F, Rahimi AR, Hadad MJ, Ashrafijou M (2014) Performance improvement of minimum quantity lubrication (MQL) technique in surface grinding by modeling and optimization. J Clean Prod 86:447–460
39. Tian WJ, Li Y, Ren JX, Yao CF (2016) Sensitivity analysis of the influence of milling parameters on the surface residual stress of titanium alloy TC11. Procedia CIRP 56:149–154
40. Yao CF, Wu DX, Tan L, Ren JX, Shi KN, Yang ZC (2013) Effects of cutting parameters on surface residual stress and its mechanism in high-speed milling of TB6. Proceedings of the institution of mechanical engineers part B. J Eng Manuf 227:483–493